REGULAR PAPER

SiC nanodot formation in amorphous-Si and poly-Si substrates using a hot-C$^+$-ion implantation technique

View the article online for updates and enhancements.

REGULAR PAPER

SiC nanodot formation in amorphous-Si and poly-Si substrates using a hot-C+-ion implantation technique

Tomohisa Mizuno[1*], Rikito Kanazawa[1], Takashi Aoki[1], and Toshiyuki Sameshima[2]

[1]Department of Science, Kanagawa University, Hiratsuka, Kanagawa 259-1293, Japan
[2]Department of Engineering, Tokyo University of Agriculture and Technology, Koganei, Tokyo 184-8588, Japan

*E-mail: mizuno@kanagawa-u.ac.jp

We experimentally studied SiC nanodot formation in an amorphous-Si (a-Si) and poly-Si on quartz substrates, using a hot-C+-ion implantation technique and post-N_2 annealing, compared with SiC-dots in a (100) crystal-Si (c-Si) on insulator substrate. Even in the poor crystal quality substrates of the C+-ion implanted in a-Si and poly-Si layers, we experimentally verified 3C-SiC dot formation by transmission electron microscopy, and the strong photoluminescence (PL) intensity in the near-UV-vis regions, because a-Si is partially poly-crystallized by the high-temperature processes of hot-C+-ion implantation and post-N_2 annealing. The PL spectral line shape strongly depends on the Si crystal structures, but the peak PL intensity after N_2 annealing is almost independent of the Si crystal structures. Moreover, the PL spectrum can be explained by the sum of PL emissions from different cubic and hexagonal polytypes of SiC. We clarified that the three Si crystal structures have a different contribution ratio of PL components of SiC polytypes. © 2019 The Japan Society of Applied Physics

1. Introduction

A two-dimensional (2D) Si layer is one of the key structures for realizing Si-based photonic devices,[1–3] because the high quantum confinement effect of electrons in 2D-Si[4–13] can modulate 2D-Si crystals into a direct-bandgap material from an indirect-bandgap three-dimensional (3D) Si.[2,10,14,15] However, the bandgap E_G and the peak photoluminescence (PL) photon wavelength λ_{PL} of (100) 2D-Si are still lower than 1.9 eV, and the PL intensity I_{PL} is too low for the Si-based visible-photonic devices.[9] Thus, we have experimentally studied the enhanced PL efficiency of the $Si_{1-Y}C_Y$ layer and SiC dots with higher E_G fabricated by a simple hot-^{12}C+-ion implantation into a (100) silicon-on-insulator (SOI) or bulk-Si substrate.[16–20] It is also reported that 3D-SiC can emit the PL photons by many recombination processes, such as, free exciton recombination,[21] except band-to-band recombination, although 3D-SiC has an indirect-bandgap structure.[22,23]

According to the self-cluster effects of ion implanted C atoms in a crystal-Si (c-Si) layer[19,24] analyzed by atom probe tomography, the C content with the C cluster size of several nm locally condenses both in the Si substrate and at the oxide/Si interface, which leads to the local formation of SiC dots in c-Si.[19,20] Corrector-spherical aberration transmission electron microscopy (CSTEM) observation and the electron diffraction (ED) patterns of the SiC dots show that 3C-SiC and hexagonal-SiC (H-SiC) dots (diameter R of several nm) are formed both at the surface-oxide (SOX)/Si interface and in the Si layer of the SOI and bulk-Si substrates.[18–20] We demonstrated the very large bandgap E_G (≈3 eV) (≡peak PL-wavelength λ_{PL} of 400 nm) and very strong PL emission I_{PL} in the near-UV-vis regions (400 < λ_{PL} < 650 nm) from the SiC dots, which is about two orders of magnitude stronger than the I_{PL} of 2D-Si.[17] Thus, the simple SiC dot technique in Si substrate is very suitable for UV-vis Si-based photonic devices.[1–3] To clarify the physical mechanism for forming SiC dots in the C+ implanted Si layer, as well as to realize low-cost Si-based photonics fabricated in low-cost Si substrates of amorphous-Si (a-Si) and poly-Si, it is strongly required that the Si crystal structure (a-Si, poly-Si and c-Si) dependence of SiC-dot formation and the PL properties be studied.

In this work, we experimentally studied SiC dot formation and the PL properties in an a-Si and poly-Si layers on quartz substrate fabricated by hot-C+-ion implantation and post-N_2 annealing.[25] We successfully formed the SiC dot formation confirmed by CSTEM images and ED patterns, and clarified the PL property of SiC dots fabricated in three Si crystal structures of a-Si, poly-Si and c-Si layers. The PL spectrum line shape as the function of the N_2 annealing time t_N and C+-ion dose D_C strongly depends on the Si crystal structures, but the peak PL intensity is almost the same between the three crystal structures. Moreover, the broad PL spectra of the three Si crystal structures can be explained by the simple model for the sum of five or four PL components of the different polytypes of cubic/hexagonal-SiC and a Si–C alloy with lower C content.

2. Experiment procedure

Figure 1 shows the fabrication steps for SiC dots in three different Si crystal structures, to evaluate the Si crystal structure dependence of SiC dots and the PL properties. After sputtering 100 nm thick SOX on Si substrate [Fig. 1(a)], Fig. 1(b) shows that hot-C+-ions were implanted into the Si substrate. The Si substrate structures used in this study are an a-Si (55 nm thick), poly-Si (20 nm thick) layer on quartz substrates, and (100)c-Si (20 nm thick) (SOI). The substrate temperature of the hot-C+-ion implantation in Fig. 1(b) was varied from 600 °C–900 °C, which are the optimum T conditions to improve the PL intensities of hot-C+-ion implanted SOI and bulk-Si substrate.[19,20] The sample just after the Fig. 1(b) step indicates SiC dots before N_2 annealing or annealing time $t_N = 0$, and the PL/Raman properties are measured before the Fig. 1(c) step. Figure 1(c) shows the additional process step of post-N_2 annealing at annealing temperature $T_N = 1000$ °C for various t_N (5 ⩽ t_N ⩽ 60 min), to poly-crystallize the a-Si layer, as well as to recover the C+ ion implantation-induced damage in Si layer, which indicate SiC dots after N_2 annealing or annealing time $t_N > 0$. In the Fig. 1(c) step, PL/Raman properties of samples are measured at every t_N. The C+ ion

© 2019 The Japan Society of Applied Physics
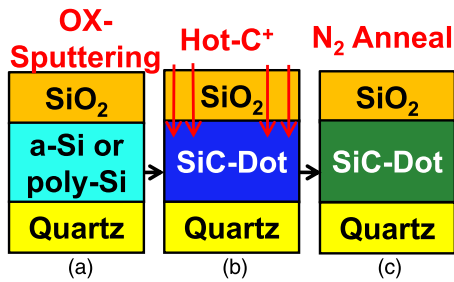
Fig. 1. (Color online) Fabrication steps for SiC dot formation in a-Si or poly-Si substrates by hot-C$^+$-ion implantation. After sputtering SiO$_2$ on a-Si or poly-Si substrates on quartz [Fig. 1(a)], Fig. 1(b) shows that hot-C$^+$-ions were implanted into Si substrates at the substrate temperature T, where $600 \leqslant T \leqslant 900$ °C and $4 \times 10^{16} \leqslant D_C \leqslant 7 \times 10^{16}$ cm^{-2} ($t_N = 0$). (c) After step (b), post-N$_2$ annealing was carried out at $T_N = 1000$ °C ($t_N > 0$), to recover the C$^+$ ion implantation-induced damage of the Si layer.
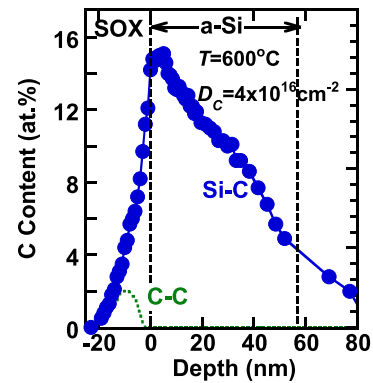
Fig. 2. (Color online) C content depth profile of Si–C (circles) and C–C bonds (dashed line) in an a-Si layer analyzed by the C1s spectrum of XPS, where $D_C = 4 \times 10^{16}$ cm^{-2}, $T = 600$ °C and $t_N = 5$ min. C content of the Si–C bond has the maximum value of 15 at% at the SOX/Si interface, and the C atoms partially separate out (2 at%) in the SOX layer. C content accuracy evaluated by XPS is about ±1 at%.

projection range was set to be the SOX/Si interface, which was confirmed by a Monte Carlo ion implantation simulator.[26,27] Since the optimum C$^+$-ion dose D_C was 4×10^{16} cm^{-2} to improve the I_{PL} in the case of c-Si,[19] D_C in this study was varied from 4×10^{16} cm^{-2} to 7×10^{16} cm^{-2}. In this study, SiC dots in the C$^+$-ion implanted a-Si, poly-Si and c-Si substrates indicate C$^+$-aSi, C$^+$-polySi and C$^+$-cSi, respectively.

PL and Raman properties of SiC dots were measured at room temperature, where the excitation laser (He-Cd) energy, laser power and laser beam diameter were 3.8 eV, 0.6 mW and 1 μm, respectively. The penetration length of the 3.8 eV laser in Si is approximately 8 nm.[17] The PL spectrum in the wide range of λ_{PL} from the near-UV to NIR regions was calibrated using a standard illuminant.[19]

3. Results and discussions

3.1. Material structures of C$^+$ implanted a-Si and poly-Si substrates

In this subsection, we clarify SiC dot formation even in an C$^+$-aSi and C$^+$-polySi, using CSTEM observation.

Figure 2(a) shows the depth profiles of C content of Si–C and C–C bonds evaluated by the C1s spectrum of X-ray photoelectron spectroscopy (XPS) after N$_2$ annealing, where $D_C = 4 \times 10^{16}$ cm^{-2}, $T = 600$ °C and $t_N = 5$ min. The C content of Si–C bond has the maximum value of 15 at% at the SOX/Si interface, and the C–C bond also shows that some C atoms of 2 at% separate out in a SOX layer. Si2p and C1s spectrum results in the C$^+$-aSi layer showed that approximately 15 at% of Si atoms binds to C atoms and 100 at% of C atoms binds to Si atoms in a-Si layer. Thus, it is expected that the maximum C content is varied from 15 at%– 26 at% at $4 \times 10^{16} \leqslant D_C \leqslant 7 \times 10^{16}$ cm^{-2} in this study. Moreover, it is found that the C content profile of C$^+$-aSi is almost the same as that of the C$^+$-ion implanted bulk-Si substrate under the same process condition.[18] Thus, it is surmised that the C content profile of C$^+$-polySi is similar to that of C$^+$-aSi, because a-Si is partially poly-crystallized during the hot-C$^+$-ion implantation process, as will be discussed later. Thus, it is expected that the peak C content at the SOX/Si interface is almost the same in the three Si crystal structures.

Figures 3(a) and 3(b) show the CSTEM images (Fig. (I)) and ED patterns [Figs. (II)–(III)] of the cross-sections of the C$^+$-aSi
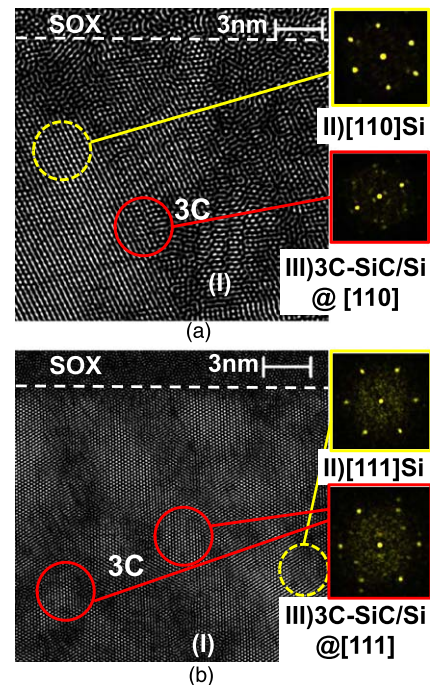
Fig. 3. (Color online) CSTEM images of (I) the cross-sections of (a) C$^+$-aSi at $t_N = 10$ min and (b) C$^+$-polySi at $t_N = 5$ min, and the ED patterns (II)–(III), where $D_C = 6 \times 10^{16}$ cm^{-2} and $T = 600$ °C. Areas encircled in red in Fig. (III) in (a) and (b) show the interference ED patterns of double layers 3C-SiC/Si in [110] C$^+$-aSi and [111] C$^+$-polySi, respectively, which is the direct verification of SiC dot formation in Si layer. 3C-SiC dot size is approximately 3 nm in both C$^+$-aSi and C$^+$-polySi. Areas encircled in dashed yellow in Fig. (II) in (a) and (b) show the ED patterns of Si in C$^+$-aSi and C$^+$-polySi, respectively.

and C$^+$-polySi surface after N$_2$ annealing, respectively, where $D_C = 6 \times 10^{16}$ cm^{-2}, $T = 600$ °C and $t_N = 10$ min. In this study, ED patterns were obtained by fast-Fourier-transform analysis of lattice spots of the CSTEM image of Figs. 3(a)(I) and 3(b)(I). Figures 3(a)(I) and 3(b)(I) show the clear lattice spots of Si atoms in both C$^+$-aSi and C$^+$-polySi. Thus, we confirmed the partial poly-crystallization of the C$^+$-aSi layer after N$_2$ annealing. Because of the random crystal direction of C$^+$-aSi and C$^+$-polySi, it was difficult to detect the SiC dots at the SOX/Si interface by CSTEM. However, Figs. 3(a)(III) and 3(b)(III) show the interference ED patterns of double layers of
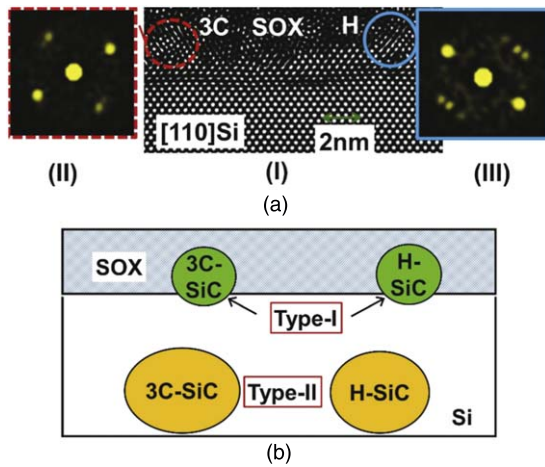
Fig. 4. (Color online) (a) (I) CSTEM image of the cross-section of the SOX/Si interface region of C^+-cSi before N_2 annealing, where $T = 900\,°C$ and $D_C = 4 \times 10^{16}\,cm^{-2}$. (II) and (III) show the ED patterns of 3C-SiC and H-SiC dots encircled by a dashed red line and blue line in (I), respectively. (b) Schematic cross-section of SiC dots in C^+-implanted Si layers. There are two types of SiC dots; Type-I and Type-II. Type-I H-SiC and 3C-SiC dots grow towards the oxide layers from the Si surface. Type-I and II dots of different SiC-polytypes can emit PL photons in a wide range of photon energy.

3C-SiC and Si in C^+-aSi and C^+-polySi, respectively, and thus, 3C-SiC dot formation in the Si layer was successfully confirmed even in poor crystal quality substrates of both the C^+-aSi and C^+-polySi layers. The 3C-SiC dot size is approximately 3 nm in both C^+-aSi and C^+-polySi.

On the other hand, it is relatively easy to observe the SiC dots even at the SOX/Si interface in the case of C^+-cSi. Actually, Fig. 4(a)(I) shows the CSTEM image of the SOX/Si interface region of C^+-cSi before N_2 annealing, where $T = 900\,°C$ and $D_C = 4 \times 10^{16}\,cm^{-2}$. Figures 4(a)(II) and 4(a)(III) show the ED patterns of 3C-SiC and H-SiC dots encircled by dashed red and blue lines in Fig. 4(a)(I), respectively. We experimentally confirmed the formation of different SiC-polytype dots even at the SOX/Si interface. The SiC dot size R at the SOX/Si interface is approximately 2 nm. Thus, it is expected that SiC dots are also formed even at the SOX/Si interface of C^+-aSi and C^+-polySi. Moreover, CSTEM analysis can distinguish 3C-SiC dots from H-SiC dots, but it is difficult for the CSTEM to determine the specific polytypes of hexagonal-SiC dots, such as 6H-SiC and 4H-SiC.

Here, we summarize SiC dots in Si substrate.[19,20] Figure 4(b) shows a schematic cross-section of SiC dots in C^+-implanted Si layers. There are two types of SiC dots; Type-I and Type-II. The Type-I of H-SiC and 3C-SiC dots grow into the SOX layer from the Si surface. Type-II dots are formed in the Si layer. It is expected that Type-I and Type-II dots of different SiC-polytypes with different E_G can emit PL photons with different peak photon energies by free exciton recombination,[21,23] which leads to the broad PL spectrum.

Next, we discuss the Raman Si-Si vibration properties of C^+-aSi, C^+-polySi and C^+-cSi, to evaluate the N_2 annealing effect on the C^+-implantation-induced damage of Si crystal quality. In addition, our previous paper[17] shows that some stacking faults of SiC dots are observed in C^+-cSi. Thus, the crystal quality of SiC dots is also evaluated by the Raman Si–C vibration mode.
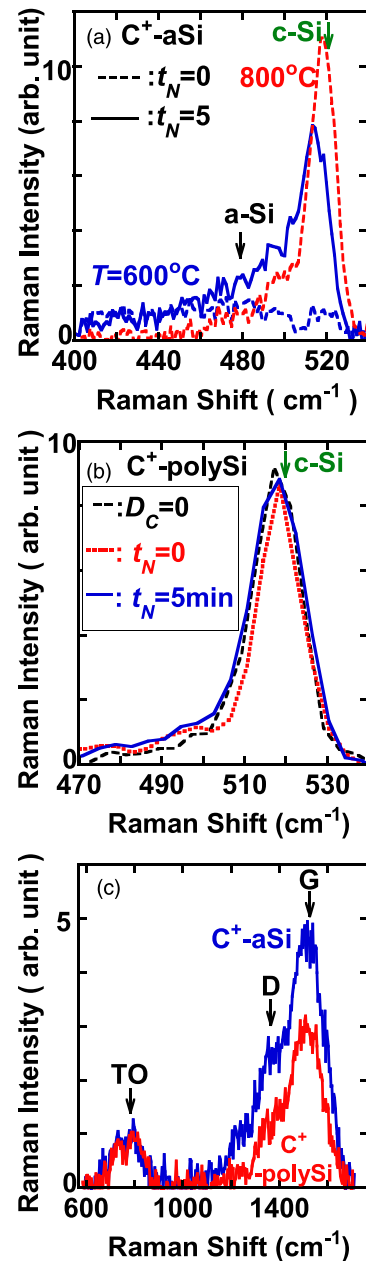
Fig. 5. (Color online) UV-Raman spectra of Si-Si vibration in (a) C^+-aSi and (b) C^+-polySi, where $D_C = 6 \times 10^{16}\,cm^{-2}$. (c) Raman spectra of the TO mode of Si–C vibration, and the G and D bands of C–C vibration in C^+-aSi (blue line) and C^+-polySi (red line), where $D_C = 6 \times 10^{16}\,cm^{-2}$ and $t_N = 10\,min$. Dotted (blue: $T = 600\,°C$, red: $T = 800\,°C$) and solid lines in (a) show the data at $t_N = 0$ and 5 min, respectively. Dashed line in (b) shows the data at $D_C = 0$. Arrows in (a) show the Raman peaks of a-Si (480 cm^{-1}) and c-Si (520 cm^{-1}). Arrows in (b) show the Raman peaks of c-Si (520 cm^{-1}). (a) shows that the C^+-aSi layer at $T = 600\,°C$ before N_2 annealing is still amorphous, but is partially poly-crystallized after short N_2 annealing. Moreover, the C^+-aSi at $T = 800\,°C$ even without N_2 annealing can also be poly-crystallized. (b) shows that the FWHM of the Si-Si vibration in C^+-polySi is affected by C^+ ion implantation and t_N.

Figures 5(a) and 5(b) show the t_N dependence of Raman spectra for Si-Si vibration in C^+-aSi and C^+-polySi, respectively, where $D_C = 6 \times 10^{16}\,cm^{-2}$. As shown in Fig. 5(a), the broad Raman spectrum with the peak of 480 cm^{-1} shows that the C^+-aSi layer at $T = 600\,°C$ before N_2 annealing ($t_N = 0$) is still amorphous. However, after short N_2 annealing at $t_N = 5\,min$, the sharp Raman spectrum of the Si-Si vibration peak of 515 cm^{-1} shows that C^+-aSi is partially poly-crystallized. Moreover, the sharp Raman peak at $T = 800\,°C$ shows
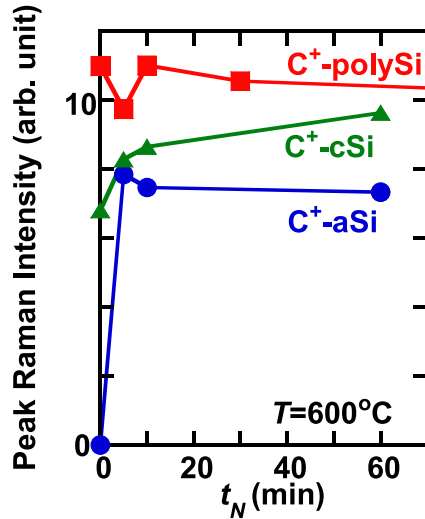
Fig. 6. (Color online) t_N dependence of Raman intensity of Si-Si vibration around 518 cm^{-1} of C$^+$-aSi (circles), C$^+$-polySi (squares) and C$^+$-cSi (triangles), where $T = 600$ °C and $D_C = 6 \times 10^{16}$ cm^{-2}. Raman intensity of C$^+$-aSi rapidly increases from zero after short N$_2$ annealing and saturates at $t_N \geqslant 5$ min, and the Raman intensity of C$^+$-cSi increases with increasing t_N. Raman intensities of C$^+$-polySi are almost constant in spite of increasing t_N.

that the C$^+$-aSi even before N$_2$ annealing ($t_N = 0$) can also be poly-crystallized by hot-C$^+$ ion implantation under high-temperature condition, which is an advantageous characteristic of the hot-C$^+$-implantation process. Thus, C$^+$-aSi can be poly-crystallized by a relatively low-temperature process.[28] On the other hand, Fig. 5(b) shows that the Raman spectra of C$^+$-polySi before ($t_N = 0$) and after N$_2$ annealing ($t_N = 5$ min) show a typical poly-Si Raman spectrum with both a Si-Si vibration peak around 517 cm^{-1} and tailing at a lower wavenumber. The FWHM before and after hot-C$^+$ ion implantation at $t_N = 0$ is 13.4 and 12.0 cm^{-1}, respectively, and the small FWHM after hot-C$^+$ ion implantation is probably attributable to the poly-Si grain size uniformity by heavy C$^+$ ion implantation. After N$_2$ annealing ($t_N = 5$ min), the FWHM of C$^+$-polySi increases to 14.5 cm^{-1} again, which suggests that the poly-Si grain size partially increases after N$_2$ annealing. On the other hand, Fig. 5(c) shows Raman spectra of the TO mode of Si–C vibration, and the G and D bands[22] of C–C vibration in C$^+$-aSi and C$^+$-polySi after N$_2$ annealing, where $D_C = 6 \times 10^{16}$ cm^{-2} and $t_N = 10$ min. However, the LO mode of Si–C vibration at 970 cm^{-1} cannot be observed, which is similar to the very small LO intensity of SiC nanoparticles ever reported.[22] The TO intensity is approximately 1/10 of the Si-Si vibration intensity shown in Figs. 5(a) and 5(b), and is too weak to study the detailed crystal quality of SiC dots (such as FWHM of TO peak) directly in this study. Moreover, the G/D band peaks also suggest the graphite formation in SOX, which is already confirmed by the C–C band of XPS data in Fig. 2. The physical mechanism for the weak Raman intensity of the Si–C vibration mode is not understood in detail, but may be due to the lower density of SiC dots; N. Namely, since N in the bulk-Si substrate was about 1×10^{12} cm^{-2},[20] the total area ($\equiv N\pi(R/2)^2$) of SiC dots with dot size R in a 1 cm^{-2} area is estimated at approximately 0.03 cm^{-2} (only 3% of Si area), which leads to the very small TO intensity of SiC dots.

Here, as shown in Fig. 6, we summarize the t_N dependence of the peak Raman intensity of the Si-Si vibration of C$^+$-aSi, C$^+$-polySi and C$^+$-cSi, where $T = 600$ °C and $D_C = 6 \times 10^{16}$ cm^{-2}. The peak Raman intensity of C$^+$-aSi at $T = 600$ °C rapidly increases after short N$_2$ annealing from zero at $t_N = 0$ and almost saturates at $t_N > 5$ min, because a-Si was partially poly-crystallized after short N$_2$ annealing, as shown in Figs. 3(a) and 5(a). Even in C$^+$-cSi, the peak Raman intensity slightly increases with increasing t_N, which indicates that the c-Si quality is slightly improved by N$_2$ annealing. However, the peak Raman intensities of C$^+$-polySi and poly-crystallized C$^+$-aSi at $t_N > 5$ min are almost saturated.

3.2. PL properties of C$^+$-aSi, C$^+$-polySi and C$^+$-cSi

In this subsection, we discuss the Si crystal structure dependence of PL properties after N$_2$ annealing.

Figures 7(a) and 7(b) show the Si crystal structure dependence of PL spectra under the same process conditions at low T of 600 °C and high T of 800 °C, respectively, where $D_C = 4 \times 10^{16}$ cm^{-2} and $t_N = 10$ min. We experimentally demonstrated the PL emission even from the poor Si crystal quality substrates of the C$^+$-aSi and C$^+$-polySi layers. The PL spectral line shape strongly depends on the Si crystal structure, namely, the PL spectrum shows the double peaks in C$^+$-aSi and C$^+$-cSi, whereas C$^+$-polySi shows a single PL peak. These PL spectral line shapes are attributable to the different PL component ratios between the three crystal structures, as discussed in the following 3.2.2 section. In addition, C$^+$-aSi shows the PL emission at the lower photon energy E_{PH} region of less than 2 eV. On the other hand, the maximum PL intensity I_{PL}; I_{MAX} strongly depends on T. Namely, the I_{MAX} of C$^+$-polySi decreases with increasing T, but the I_{MAX} of C$^+$-cSi drastically increases with increasing T. Therefore, the optimum T for improving I_{MAX} is very different between C$^+$-cSi and C$^+$-aSi/C$^+$-polySi. Hereafter, we mainly discuss the PL properties under optimum low T condition for C$^+$-aSi/C$^+$-polySi.

Here, the I_{PL} of SiC dots can be given by the following equation[20,29]:

$$I_{PL} \propto \eta(R)S \propto \eta(R)NR^2 \propto \frac{\tau}{\tau_R}NR^2, \qquad (1)$$
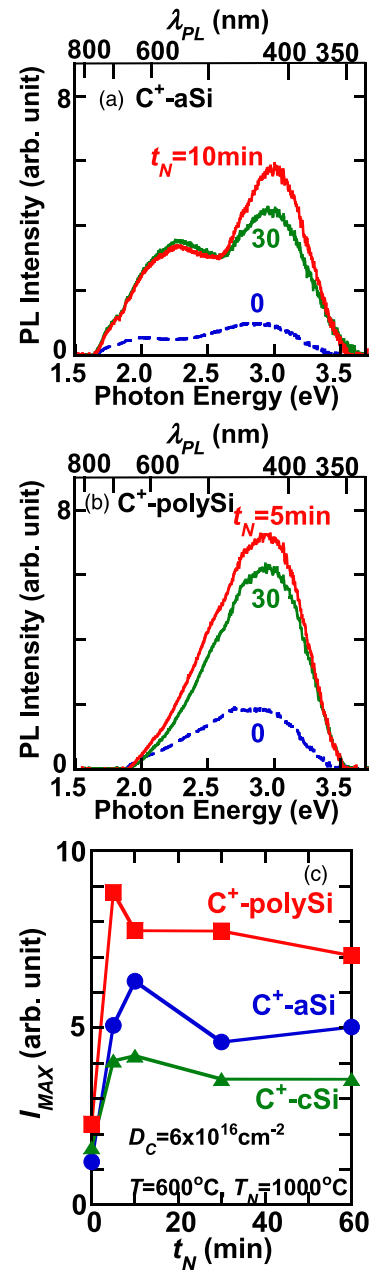
where R is the SiC dot size, S is the total area of SiC dots in a unit area, N is the SiC dot density, $\eta(R)$ is the PL quantum efficiency of SiC dot, and τ and τ_R are the excited electron life time and radiative life time, respectively.[20,29] The $\eta(R)$ increases by improving the semiconductor crystal quality, because of the improved τ.[19] In addition, to increase the PL intensity, it is strongly required to increase the SiC dot density. On the other hand, when the SiC dots are quantum dots, $\eta(R)$ also increases with reducing R, because of enhanced Heisenberg uncertainty of electron wavenumber in smaller SiC dot.[22] As a result, the peak PL energy E_{PH} of SiC quantum dots strongly depends on R, because the E_G of spherical SiC quantum dots is proportional to R^{-2}.[29] Thus, when the SiC quantum dot size decreases, the E_{PH} of the PL spectrum rapidly increases,[22] but Eq. (1) shows that the I_{PL} is determined by the balance between the $\eta(R)$ improvement and S ($\propto R^2$) reduction at smaller R.

3.2.1. Process dependence of PL. First, we discuss the t_N dependence of PL properties of SiC dots.
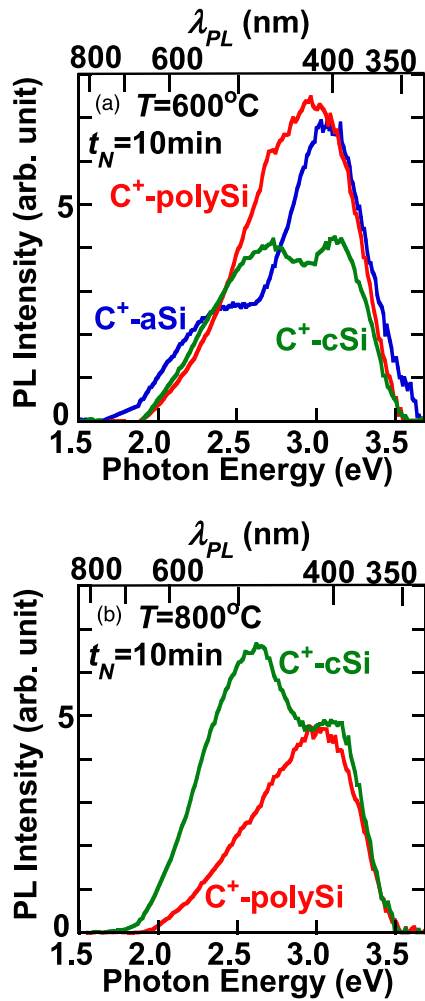
Fig. 7. (Color online) SiC-dot PL spectrum comparison between C^+-aSi (blue), C^+-polySi (red) and C^+-cSi (green) at (a) $T = 600\,°C$ and (b) $T = 800\,°C$, where $D_C = 4 \times 10^{16}\,cm^{-2}$ and $t_N = 10$ min. Lower and upper lateral axes show a PL photon energy and wavelength, respectively. PL spectral line shape strongly depends on the Si crystal structure even under the same process conditions. Only C^+-aSi has the PL emission at lower photon energy less than 2 eV. Moreover, (a) and (b) show that PL spectra of C^+-polySi and C^+-cSi strongly depend on T.

Fig. 8. (Color online) t_N dependence of PL spectra of (a) C^+-aSi and (b) C^+-polySi, and (c) I_{MAX} of C^+-aSi (circles), C^+-polySi (squares) and C^+-cSi (triangles), where $D_C = 6 \times 10^{16}\,cm^{-2}$ and $T = 600\,°C$. PL spectrum and intensity of both C^+-aSi and C^+-polySi strongly depend on t_N. (c) shows that the I_{MAX} of the three SiC dots drastically increases at $t_N \approx 5$ min, but almost saturates at $t_N \geqslant 30$ min.
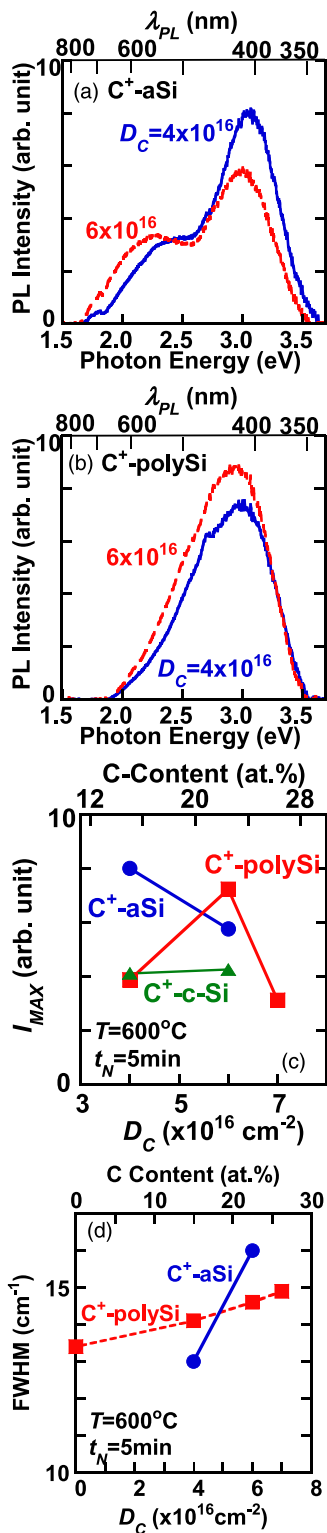
Figures 8(a) and 8(b) show the t_N dependence of PL spectra of C^+-aSi and C^+-polySi under the same process conditions, respectively, where $D_C = 6 \times 10^{16}\,cm^{-2}$ and $T = 600\,°C$. Even from C^+-aSi before N$_2$ annealing, small PL emission was observed in Fig. 8(a), which suggests that some SiC dots are formed even in an a-Si layer. However, the PL intensity of C^+-aSi before N$_2$ annealing was much lower than that of C^+-polySi before N$_2$ annealing, which is attributable to the poorer crystal quality of C^+-aSi at $t_N = 0$. The PL intensity in both structures strongly depends on t_N, and rapidly increases after short N$_2$ annealing. However, the PL spectral line shape is almost independent of t_N. Moreover, Fig. 8(c) shows the t_N dependence of the maximum PL intensity I_{MAX} of C^+-aSi, C^+-polySi and C^+-cSi, as the same process conditions in Figs. 8(a) and 8(b). The I_{MAX} of the three structures strongly depends on t_N, rapidly increases after short N$_2$ annealing of $0 < t_N \leqslant 10$ min, and almost saturates at $t_N > 10$ min, the physical mechanism of which is discussed in Sect. 3.2.2. The $I_{MAX}(t_N)$ enhancement factors of C^+-aSi, C^+-polySi and C^+-cSi, compared with $I_{MAX}(0)$, reach 5.8, 3.9 and 2.6 at $t_N \approx 10$ min,
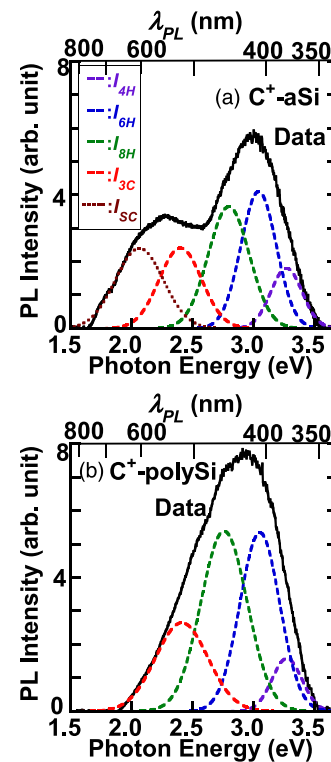
respectively. The larger I_{MAX} enhancement factor of 5.8 in C^+-aSi is attributable to the large improvement of PL intensity of poly-crystallized C^+-aSi after short N$_2$ annealing.

Second, Figs. 9(a) and 9(b) show the D_C dependence of the PL spectra of C^+-aSi at $t_N = 10$ min and C^+-polySi at $t_N = 5$ min, respectively, where $T = 600\,°C$. The PL intensity of both C^+-aSi and C^+-polySi strongly depend on D_C, too. The optimum D_C to improve the PL intensity is different between C^+-aSi and C^+-polySi. However, the PL spectral line shapes of C^+-aSi and C^+-polySi are almost independent of D_C. Here, Fig. 9(c) shows the D_C dependence of I_{MAX}. C^+-polySi has the maximum PL intensity at $D_C = 6 \times 10^{16}\,cm^{-2}$, whereas C^+-aSi and C^+-cSi have the peak PL intensity at $D_C = 4 \times 10^{16}\,cm^{-2}$. The physical

Fig. 10. (Color online) PL component (Gaussian curve (dashed lines)) fittings for the measured PL spectra (solid lines) of (a) C$^+$-aSi and (b) C$^+$-polySi, where $D_C = 6 \times 10^{16}$ cm^{-2}, $T = 600$ °C and $t_N = 10$ min. Measured PL of C$^+$-polySi can possibly be explained by the sum of PL emissions from four different SiC-polytypes of 3C-SiC (I_{3C}: red), 8H-SiC (I_{8H}: green), 6H-SiC (I_{6H}: blue) and 4H-SiC (I_{4H}: purple), but the PL of C$^+$-aSi originates from an additional one-component of Si–C alloy I_{SC} (brown) with lower E_G, as well as the above four different SiC-polytypes.

slightly increases with increasing D_C, which indicates that the crystal quality of the Si substrate is slightly degraded by the high D_C-induced damage in Si.

3.2.2. PL components of SiC polytypes. The above TEM analyses in Figs. 3 and 4 show that the SiC dots consist of cubic and hexagonal-SiC dots. Thus, the broad PL spectrum with the PL energy from 2–3.5 eV, shown in Figs. 7 and 8, is possibly explained by the simple model for the sum of PL emissions by free exciton recombination from different SiC-polytypes with different exciton gap E_{GX}.[17,19,20,23] Generally, SiC has many polytypes with different E_{GX}. Thus, in this study, we assume the typical SiC polytypes of 3C-, 8H-, 6H- and 4H-SiC, considering the range and space of E_{GX} in SiC polytypes. As a result, the E_{GX} of SiC dots increases from 2.39 eV of 3C-SiC to 3.27 eV of 4H-SiC with increasing the hexagonality.[23] In this subsection, we discuss the physical mechanism for broad PL spectra of SiC dots in three Si crystal structures.

Figures 10(a) and 10(b) show Gaussian curve fittings of PL components for the measured PL spectra of C$^+$-aSi and C$^+$-polySi, respectively, where $D_C = 6 \times 10^{16}$ cm^{-2}, $T = 600$°C and $t_N = 10$ min. The measured broad PL spectra of C$^+$-aSi and C$^+$-polySi can be explained by the sum of PL emissions of different SiC-polytype dots of 3C-SiC intensity (I_{3C}) with E_{GX} of 2.39 eV (E_{3C}), 8H-SiC intensity (I_{8H}) with E_{GX} of 2.73 eV (E_{8H}), 6H-SiC intensity (I_{6H}) with E_{GX} of 3.02 eV (E_{6H}) and 4H-SiC intensity (I_{4H}) with E_{GX} of 3.27 eV (E_{4H}),[20,23] assuming that the binding energy of free

Fig. 9. (Color online) D_C dependence of the PL spectra of (a) C$^+$-aSi at $t_N = 10$ min and (b) C$^+$-polySi at $t_N = 5$ min, (c) I_{MAX}, and (d) FWHM of Si-Si vibration Raman peak, where $T = 600$ °C. Circles, squares and triangles in (c) show the I_{MAX} of C$^+$-aSi, C$^+$-polySi and C$^+$-cSi, respectively. In (d), circles and squares show the FWHM of C$^+$-aSi and C$^+$-polySi, respectively, and the upper lateral axis shows the estimated peak C content at the SOX/Si interface. PL intensity of all SiC strongly depend on D_C, too. (d) shows that the FWHM slightly increases with increasing D_C.

mechanism for the D_C dependence of PL intensity is discussed in Sect. 3.2.2. On the other hand, Fig. 9(d) shows the D_C dependence of the FWHM of Si-Si Raman peak in C$^+$-aSi and C$^+$-polySi. The FWHM of both structures
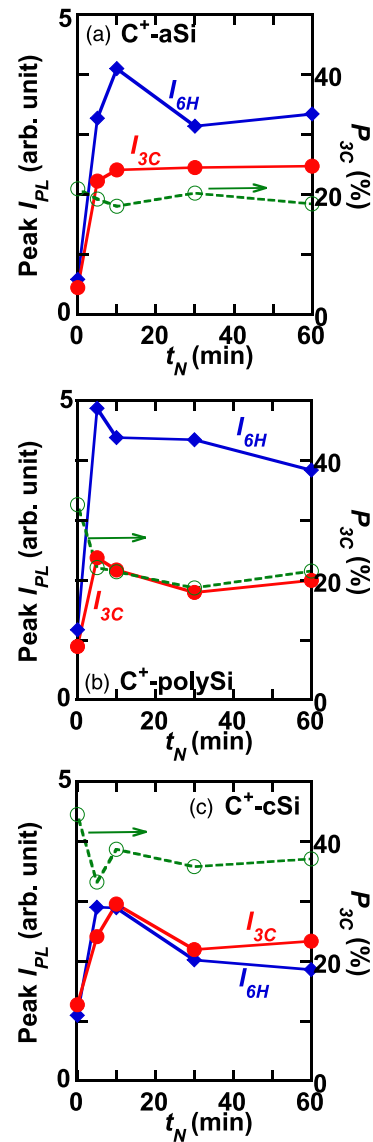
excitons is approximately 20 meV.[23] Moreover, the PL component with lower E_G in C$^+$-aSi (I_{SC}) possibly originates from the PL emission of Si–C alloy with lower C content and lower E_G,[16,30] since previous works[16,30] showed that the PL intensity and E_G of Si–C alloy drastically increase with increasing the C content. In addition, no SiC polytype with E_G of lower than 2.4 eV does not exist.[22,23] Thus, only C$^+$-aSi shows an imperfect silicon carbide formation like a Si–C alloy. However, the 2H-SiC polytype with the hexagonality of 100% and higher E_G of 3.33 eV[22] cannot be observed by fitting curve for the measured PL spectrum in this study. Moreover, the PL component ratio of C$^+$-aSi is very different to that of C$^+$-polySi, since the ratio of I_{8H} and I_{6H} components is very high in C$^+$-polySi.

First, we show the t_N dependence of the main cubic and hexagonal PL components of peak-I_{3C} and peak-I_{6H}. Figures 11(a)–11(c) show the t_N dependence of the PL components of C$^+$-aSi, C$^+$-polySi and C$^+$-cSi, respectively, where $D_C = 6 \times 10^{16}$ cm^{-2} and $T = 600°$C. Almost all peak-I_{PL} components are the same as the t_N dependence of I_{MAX} shown in Fig. 8(c), and rapidly increase at $t_N \approx 5$ min, too. In addition, the I_{3C} of C$^+$-aSi is almost the same as the I_{3C} of C$^+$-polySi, whereas the I_{6H} is much higher than I_{3C} in both C$^+$-aSi and C$^+$-polySi. On the other hand, Fig. 11(c) shows that the I_{3C} of C$^+$-cSi is almost the same as I_{6H} of C$^+$-cSi and I_{3C} of C$^+$-aSi and C$^+$-polySi. Here, we estimate the total photon emission number from each PL component, which is an indicator for each polytype ratio of SiC. The ratio of PL spectrum component I_I to total I_{PL} emission; P_I (subscript I is from SC to 4H) can be precisely determined by the integrated I_I divided by the total integrated I_{PL} in the whole range of photon energy E. Namely,

$$P_I = \frac{\int I_I dE}{\int I_{PL} dE}. \tag{2}$$

Fig. 11. (Color online) t_N dependence of peak-I_{3C} and I_{6H} of (a) C$^+$-aSi, (b) C$^+$-polySi and (c) C$^+$-cSi, where $D_C = 6 \times 10^{16}$ cm^{-2} and $T = 600$ °C. Closed rhombi and circles show I_{6H} and I_{3C}, respectively, and all SiC-polytype components are almost the same as the t_N dependence of I_{MAX}. Open circles (right vertical axis) show the P_{3C} of Eq. (2). (a) and (b) show that P_{3C} is a constant of approximately 20% in both C$^+$-aSi and C$^+$-polySi, and thus the hexagonal components of SiC in both C$^+$-aSi and C$^+$-polySi are much higher than the cubic components of SiC. However, (c) shows that the P_{3C} of C$^+$-cSi is very high and a constant of approximately 40%.

Figures 11(a) and 11(b) show that P_{3C} is a constant of approximately 20% in both C$^+$-aSi and C$^+$-polySi, and thus the hexagonal components of SiC are much higher than the cubic SiC component. Thus, in both C$^+$-aSi and C$^+$-polySi, the 8H-SiC and 6H-SiC components are the main PL emission. However, the P_{3C} of C$^+$-cSi is about twice the P_{3C} of C$^+$-aSi and C$^+$-polySi, and is a constant of approximately 40%, and thus the cubic SiC dot formation rate is high only in C$^+$-cSi.

Next, Figs. 12(a) and 12(b) show the t_N dependence of the fitting peak PL energy E_{PH} of each PL component of C$^+$-aSi and C$^+$-polySi, respectively, where $D_C = 6 \times 10^{16}$ cm^{-2} and $T = 600$ °C. The peak-E_{PH} of each SiC-polytype in both Si structures is almost the same as the experimental E_{GX} of the 3D-SiC polytypes,[23] and is independent of t_N. This constant peak-E_{PH} was also confirmed in C$^+$-cSi. The maximum E_{PH} variation in this study was approximately 0.05 eV and very small. When the SiC dots are quantum dots, it is reported[22] that the E_G of SiC quantum dots rapidly increases with reducing R at $R < 4$ nm, which leads to the rapid increase of PL intensity. As a result, Fig. 12 data suggest that the SiC dots in this study are not quantum dots. Moreover, our previous work[20] shows that Type-II dot density in C$^+$ implanted bulk-Si substrate decreases after N$_2$ annealing.

Therefore, another analogical-mechanism for the N$_2$ anneal-induced I_{PL} improvement is the crystal uniformity and defect reduction of SiC dots after N$_2$ annealing. On the other hand, the E_{SC} of approximately 2.1 eV in C$^+$-aSi is equivalent to the E_G of 3D Si–C alloy with the C content of approximately 2.5 at%.[16,17,30]

Second, we show the D_C dependence of the main PL components of peak-I_{3C} and peak-I_{6H} in the three Si crystal structures. Figures 13(a) and 13(b) show the D_C dependence of I_{6H} and I_{3C}, respectively, where $T = 600°$C and $t_N = 10$ min. First, the D_C dependence of peak-I_{6H} and I_{3C} is different between the three Si structures. C$^+$-polySi and C$^+$-cSi have the maximum PL component intensity at $D_C = 6 \times 10^{16}$ cm^{-2}, whereas C$^+$-aSi has the peak PL intensity at $D_C = 4 \times 10^{16}$ cm^{-2}. This D_C dependence difference between the three Si crystal structures is not physically
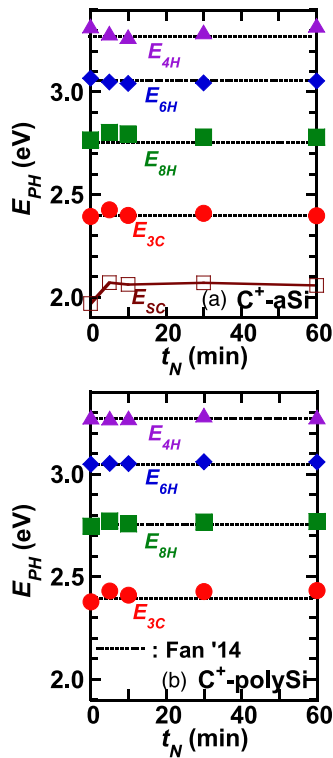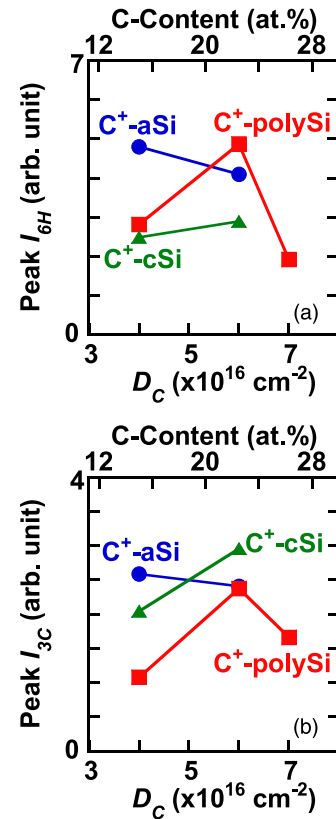
Fig. 12. (Color online) t_N dependence of peak-E_{PH} of each different PL component in (a) C$^+$-aSi and (b) C$^+$-polySi, where $D_C = 6 \times 10^{16}$ cm^{-2} and $T = 600$ °C. Dashed lines show the experimental E_{GX} of each different 3D-SiC polytype ever reported.[22, 23] Triangles, rhombi, squares, circles and open-squares show the peak-E_{PH} of I_{4H}, I_{6H}, I_{8H}, I_{3C} and I_{SC}, respectively, which are almost independent of t_N.


Fig. 13. (Color online) D_C dependence of (a) I_{6H} and (b) I_{3C} of C$^+$-aSi (circles), C$^+$-polySi (squares) and C$^+$-cSi (triangles) under the optimum conditions of t_N, where $T = 600$°C. Upper lateral axis shows the peak C content at the SOX/Si interface. C$^+$-polySi and C$^+$-cSi have the maximum PL intensity at $D_C = 6 \times 10^{16}$ cm^{-2}, whereas C$^+$-aSi has the peak PL intensity at $D_C = 4 \times 10^{16}$ cm^{-2}. It is noted that (c) shows higher I_{3C} of C$^+$-cSi.

understood at present. On the other hand, similar to the t_N dependence of the peak-E_{PH} of each PL component shown in Fig. 12, the peak-E_{PH} of each PL component was almost independent of D_C, too. It is considered that the SiC dot density increases with increasing D_C, which leads to PL intensity improvement of C$^+$-polySi and C$^+$-cSi at $D_C \leqslant 6 \times 10^{16}$ cm^{-2}. However, the I_{6H} and I_{3C} reduction of C$^+$-polySi at $D_C = 7 \times 10^{16}$ cm^{-2} is possibly due to the poly-Si quality reduction shown as the FWHM degradation of Si-Si vibration in Fig. 9(c). Therefore, the D_C dependence of PL intensity is probably caused by the balance between the D_C dependence of dot density N and η in Eq. (1).

3.2.3. Crystal structure dependence of PL intensity under optimum process conditions. The above discussions and our previous works[19] show that the optimum process conditions of T, t_N and D_C for improving PL intensity are different between the three Si crystal structures. In this subsection, we compare the maximum PL intensities of the three Si crystal structures under the individual optimum process conditions.

Figure 14(a) shows the maximum PL spectrum comparison between the three crystal structures under each optimum process condition. The optimum T of C$^+$-aSi, C$^+$-polySi and C$^+$-cSi is 600 °C, 600 °C and 800 °C, respectively. In addition, the optimum t_N of C$^+$-aSi, C$^+$-polySi and C$^+$-cSi is 5, 5 and 30 min, respectively, and the optimum D_C of C$^+$-aSi, C$^+$-polySi and C$^+$-cSi is 4×10^{16}, 6×10^{16}, 4×10^{16} cm^{-2}, respectively. The maximum PL intensity of the three Si crystal structures is almost the same, since the I_{MAX} variation between the three structures is only ±12%. On

the other hand, the PL spectral line shape strongly depends on the Si crystal structure, because of the different PL component ratio in the three Si crystal structures. However, only C$^+$-cSi shows that the peak PL intensity at a lower E_{PH} of 2.5 eV is higher than that at a higher E_{PH} of 3.1 eV, which can be explained by the high ratio of P_{3C} shown in Figs. 11(c) and 14(b). Moreover, Fig. 14(b) shows the ratio of each integrated PL intensity of the PL components obtained by Eq. (2) with the same data of Fig. 14(a), and the PL component ratio of C$^+$-aSi and C$^+$-polySi is very different to that of C$^+$-cSi. C$^+$-aSi and C$^+$-polySi show that the total ratio of the hexagonal PL components from P_{8H} to P_{4H} is higher than 75%, whereas C$^+$-cSi shows that the cubic PL component P_{3C} is higher than 40%. Thus, the cubic SiC structure formation rate is higher in a single-crystal Si structure. However, the C$^+$-aSi characteristics are the only Si–C alloy dot formation with the ratio of 9%, and P_{4H} to P_{8H} are almost constant in a range of about 20%. The main PL emissions of C$^+$-polySi are P_{8H} and P_{6H} in a range of 30%. Consequently, Fig. 14(b) suggests that the formation ratio of SiC-polytypes can be partly controlled by the Si crystal structure.

4. Conclusion

In this work, we experimentally clarified the three Si crystal structure dependence of SiC dot formation and the PL properties, using the hot-C$^+$-ion implantation technique and
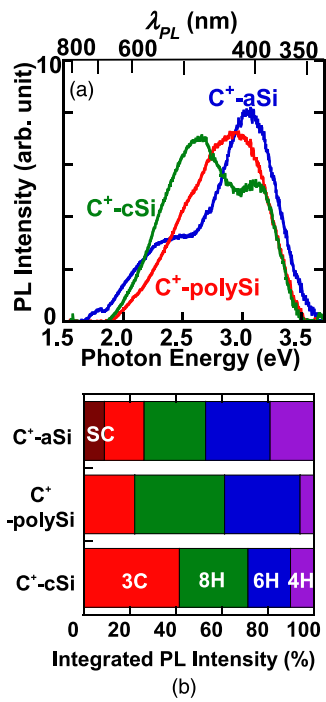
Fig. 14. (Color online) (a) PL spectrum comparison between three Si crystal structures each under optimum process condition. Peak-I_{PL} is almost independent of the Si crystal structure, but the PL spectral line shape strongly depends on the Si crystal structure. (b) Ratio of integrated PL intensities of each PL component; P_{4H}, P_{6H}, P_{8H}, P_{3C} and P_{SC} of Eq. (2) in C$^+$-aSi, C$^+$-polySi and C$^+$-cSi under an individual optimum process condition. Hexagonal components of C$^+$-aSi and C$^+$-polySi are higher than 70%, whereas the cubic component of C$^+$-cSi exceeds 40%.

post-N$_2$ annealing. Even in the poor Si quality of the C$^+$-aSi and C$^+$-polySi layers, CSTEM analyses confirmed a SiC dot formation, and we demonstrated the very strong PL intensities of C$^+$-aSi and C$^+$-polySi, which are considered to be mainly attributable to the free exciton recombination process[21] in SiC dots.

CSTEM and ED pattern data of the cross-section of the hot-C$^+$-ion implanted three Si crystal structures showed that 3C-SiC dots are formed in the Si layer, and especially in C$^+$-cSi, 3C-SiC and H-SiC dot formation are also verified at the SOX/Si interface. Thus, it is found that two types of SiC dots coexist. Type-I SiC dot at the SOX/Si interface is a dot which is partially embedded in SOX. Type-II SiC dots exist in the Si layer. It is expected that these Type-I and II dots can emit PL photons. Moreover, CSTEM and UV-Raman spectroscopy showed that the C$^+$-aSi layer was partially polycrystallized after short N$_2$ annealing or by hot-C$^+$-ion implantation at high temperature.

The PL spectral line shape in the wide range of near-UV-vis regions strongly depends on the Si crystal structure, and the PL intensity of the three Si crystal structures rapidly increases after short N$_2$ annealing, which may be caused by the crystal uniformity and defect reduction of SiC dots after short N$_2$ annealing. Even in an amorphous-Si before N$_2$ annealing at low T, we confirmed the PL emission, which suggests that some SiC dots are partially formed even in an amorphous-Si layer. Moreover, the PL intensity also depends on the C$^+$ dose, and the optimum C$^+$ dose exists to improve the PL intensity.

The broad PL spectrum of the three Si crystal structures can possibly be explained by the simple model for the sum of

the PL component emissions from four different polytypes of 3C-SiC, 8H-SiC, 6H-SiC and 4H-SiC dots in C$^+$-ion implanted Si substrate, and the PL of C$^+$-aSi originates from an additional one-component of Si–C alloy with lower E_G, as well as four different SiC-polytypes. The PL component intensities of the three crystal structures strongly depend on the N$_2$ annealing time and C$^+$ dose. However, the PL peak energies of the PL components are almost independent of the N$_2$ annealing time and C$^+$ dose. Thus, the PL intensity improvement is possibly caused by the crystal uniformity and defect reduction of SiC dots after N$_2$ annealing or SiC dot density increase at high C$^+$ dose.

The ratio of integrated PL intensities of each PL component is an indicator for the dot formation rate of each SiC-polytype. C$^+$-aSi and C$^+$-polySi show that the ratio of hexagonal PL components is higher than 75%, whereas C$^+$-cSi shows that the cubic PL component is higher than 40%. Thus, the cubic SiC structure formation rate is higher in a single-crystal Si structure. However, the C$^+$-aSi characteristics are the only Si–C alloy dot formation with the ratio of 9%.

The three crystal structures have different optimum process conditions to improve the PL intensity. The maximum PL intensity is almost independent of the Si crystal structures. Consequently, the hot-C$^+$-ion implantation process for low-cost substrates of a-Si and poly-Si is very promising for low-cost Si-based photonic devices.

Acknowledgment

1) S. Saito et al., Jpn. J. Appl. Phys. **45**, L679 (2006).
2) S. Saito et al., IEDM Tech. Dig., 2008, p. 19.5.
3) L. Pavesi and D. J. Lockwood, *Silicon Photonics* (Springer, Berlin, 2004).
4) T. Mizuno, K. Tobe, Y. Maruyama, and T. Sameshima, Jpn. J. Appl. Phys. **51**, 02BC03 (2012).
5) T. Mizuno, T. Aoki, Y. Nagata, Y. Nakahara, and T. Sameshima, Jpn. J. Appl. Phys. **52**, 04CC13 (2013).
6) T. Mizuno, Y. Nakahara, Y. Nagata, Y. Suzuki, T. Aoki, and T. Sameshima, Jpn. J. Appl. Phys. **53**, 04EC08 (2014).
7) T. Mizuno, Y. Nagata, Y. Suzuki, Y. Nakahara, T. Aoki, and T. Sameshima, Jpn. J. Appl. Phys. **53**, 04EC09 (2014).
8) T. Mizuno, Y. Nagamine, Y. Suzuki, Y. Nakahara, Y. Nagata, T. Aoki, and T. Sameshima, Jpn. J. Appl. Phys. **54**, 04DC05 (2015).
9) T. Mizuno, Y. Suzuki, Y. Nagamine, Y. Nakahara, Y. Nagata, T. Aoki, and T. Maeda, Jpn. J. Appl. Phys. **54**, 04DC02 (2015).
10) L. Donetti, F. Gámiz, J. B. Roldán, and A. Godoy, J. Appl. Phys. **100**, 013701 (2006).
11) K. Uchida, H. Watanabe, A. Kinoshita, J. Koga, T. Numata, and S. Takagi, IEDM Tech. Dig., 2002, p. 47.
12) K. Uchida, J. Koga, and S. Takagi, J. Appl. Phys. **102**, 074510 (2007).
13) G. Tsutsui, M. Saitoh, and T. Hiramoto, IEEE Trans. Electron Devices **26**, 836 (2005).
14) B. K. Agrawal and S. Agrawal, Appl. Phys. Lett. **77**, 3039 (2000).
15) S. S. Iyer and Y.-H. Xie, Science **260**, 40 (1993).
16) T. Mizuno, Y. Nagamine, Y. Omata, Y. Suzuki, W. Urayama, T. Aoki, and T. Sameshima, Jpn. J. Appl. Phys. **55**, 04EB02 (2016).
17) T. Mizuno, Y. Omata, Y. Nagamine, T. Aoki, and T. Sameshima, Jpn. J. Appl. Phys. **56**, 04CB03 (2017).
18) T. Mizuno, S. Nakada, M. Yamamoto, S. Irie, Y. Omata, T. Aoki, and T. Sameshima, Extended Abst. of Solid State Devices and Materials, 2017, p. 597.
19) T. Mizuno, Y. Omata, R. Kanazawa, Y. Iguchi, S. Nakada, T. Aoki, and T. Sasaki, Jpn. J. Appl. Phys. **57**, 04FB03 (2018).

20) T. Mizuno, S. Nakada, M. Yamamoto, S. Irie, T. Aoki, and T. Sameshima, Abst. IEEE Silicon Nanoelectronics Workshop, 2018, p. 121.

21) T. Kimoto, S. Nakazawa, K. Hashimoto, and H. Matsunami, Appl. Phys. Lett. **79**, 2761 (2001).

22) J. Fan and P. K. Chu, *Silicon Carbide Nanostructure* (Berlin), (Springer, 2014), Chap. 2, Chap. 4.

23) T. Kimoto and J. A. Cooper, *Fundamentals of Silicon Carbide Technology* (IEEE Press, Singapore, 2014), Chap. 2., Chap. 5.

24) Y. Shimizu et al., Appl. Phys. Lett. **98**, 232101 (2011).

25) T. Mizuno, R. Kanazawa, Y. Omata, T. Aoki, and T. Sameshima, Extended Abst. of Solid State Devices and Materials, 2018, p. 803.

26) J. F. Ziegler [http://srim.org/].

27) http://silvaco.com/.

28) I.-W. Wu, A. G. Lewis, T.-Y. Huang, and A. Chiang, IEEE Electron Device Lett. **10**, 123 (1989).

29) S. M. Sze and K. K. Ng, *Physics of Semiconductor Devices* (Wiley, New York, 2007), Chap. 1, Chap. 12, Chap. 14.

30) L. R. Tessler and I. Solomon, Phys. Rev. B **52**, 10962 (1995).